



Liquid bismuth initiated growth of phosphorus microbelts with efficient charge polarization for photocatalysis



Yang Liu^a, Zhuofeng Hu^{b,*}, Jimmy C. Yu^{a,*}

^a Department of Chemistry, The Chinese University of Hong Kong, Shatin, New Territories, 999077, Hong Kong, China

^b School of Environmental Science and Engineering, Guangdong Provincial Key Laboratory of Environmental Pollution Control and Remediation Technology, Sun Yat-sen University, Guangzhou, 510275, China

ARTICLE INFO

Keywords:

Red phosphorus
Elemental photocatalyst
Charge polarization
Hydrogen evolution
Organic pollutant degradation

ABSTRACT

Charge polarization is an interesting and vital phenomenon in nature. This is the first report of such effect in crystalline red phosphorus (P). We synthesized large-scale (up to $100 \times 10 \times 0.3 \mu\text{m}^3$) single crystal red P microbelts (PMBs) in the presence of bismuth (Bi) nanodroplets via a thermal vaporization method. Under visible light illumination, the PMBs become highly polarized. Electrons accumulate at the two ends of the microbelts which become negatively charged, while the middle section is positive. In an aqueous solution, the PMBs can trigger water reduction to produce hydrogen at their negative-charged ends. Compared with where charge carriers are randomly distributed, the highly-polarized PMBs exhibit ten times enhancement in photocatalytic hydrogen production. An explanation for this interesting light-induced polarization effect is provided based on experimental results and theoretical calculations. This work may shed new light on the future development of high-efficiency P-based photocatalytic devices and systems.

1. Introduction

Charge polarization serves special purposes in nature. In brain cells, the inside is negatively charged and the outside is positively charged. This arrangement plays a crucial role in the signal transmission through neurons; and polarization also play an important role in controlling the rhythmic activity of cardiac pacemaker cells [1,2]. The polarization phenomenon is very useful in industry. A good example is the electric polarization in ferroelectrics [3]. These materials are indispensable in many memory devices, capacitors, and sensors. In the field of catalysis, charge polarization can promote the transfer of charge carriers and therefore speeds up chemical reaction [4–8]. Take a hybrid catalyst MoS₂/Pd as an example, an interfacial charge polarization between MoS₂ and Pd can increase electron density of the S sites and thus enhances H₂ evolution activity [9]. Some comprehensive studies were published regarding the charge transfer in heterogeneous photocatalysts, but relatively little emphasis has been placed on the effect in elemental systems [10–14]. Herein, we report the first observation of a photo-induced charge polarization effect in a pure elemental substance, crystalline red phosphorus microbelts (PMBs). Under illumination, the two ends of the PMBs become negatively charged, while the middle section is positive.

Phosphorus (P) is one of the most abundant and versatile elements

in the earth's crust. Since its discovery in 1669 [15], much effort has been devoted to synthesis and analysis of different P allotropes, such as Hittorf P [16,17], fibrous P [18], type-II P [19], and Black P [20,21]. Phosphorus has been widely used in the fields of battery [22], field-effect transistor, supercapacitance, and photocatalytic system [23]. The investigation of elemental P as a semiconductor is one of the hottest topics in material science [24–26]. In many systems, especially in photocatalysis, the electronic structure, and charge transfer property are closely related to photon utilization and the activity of the catalysts. For example, two-dimensional black P has much higher charge mobility than its bulk counterpart, leading to better performance in H₂ evolution [27]. Crystalline red P with higher charge transfer efficiency is more competitive than amorphous one in photocatalysis [26,28,29]. However, there are hardly any reports about charge polarized P. We expect that the charge polarization will increase the electron density on specific regions of P crystal, which could serve as reaction sites for photocatalytic reduction reaction, such as H₂ evolution. Compared with a random distribution of photo-excited charge, polarized charge attributes to less charge recombination and higher charge transfer efficiency.

We synthesized highly charge polarized single crystalline red PMBs with the assistant of liquid bismuth (Bi) nanodroplets. Typically, the temperature is first elevated to 550 °C to enable the vaporization of

* Corresponding authors.

E-mail addresses: huzhf8@mail.sysu.edu.cn (Z. Hu), jimyu@cuhk.edu.hk (J.C. Yu).

amorphous red P and to melt of Bi, and then declined and kept at 300 °C for 10 h. P condenses at this temperature and grow to form microbelts with the assistant of liquid Bi nanodroplets. Finally, the large-sized single crystalline red PMBs (up to $100 \times 10 \times 0.3 \mu\text{m}^3$) are obtained and indexed to Hittorf's P. The high crystallinity is conducive to effective charge transfer in the photocatalyst. Importantly, we discovered the charge polarization in the crystal. The photoexcited electrons preferentially move to the short edges ((013) facets) under illumination. This is evidenced by facet-selective photo-deposition of Pt on (013) facets and surface potential distribution along the microbelts in KPFM measurement. Besides, first principle calculation suggests that there are intermediate states below the conduction band (CB) on (013) facets of Hittorf's P. Electrons in CB will migrate from the CB to the 013 facet thermodynamically, leading to the polarization of the red P. Decomposed charge density map also indicates the preferential accumulation of electrons on the (013) facets. As a result, the activity of the as-prepared red PMBs is ten times higher than that of amorphous red P for photocatalytic H₂ evolution and three times higher for methyl orange (MO) degradation.

2. Experimental

2.1. Preparation of red PMBs

Amorphous red P was purified from commercial red phosphorus via a hydrothermal method to remove surface oxide. Commercial red P was dispersed in D.I. water, put into a Teflon-lined stainless autoclave, and heated at 200°C for 12 h. After washing with D.I. water and ethanol, amorphous red P was obtained. 300 mg of purified red P and 60 mg of Bi powder were sealed in vacuum quartz capsules (10 cm in length and 1 cm in diameter). Other samples with 300 mg red P and different mass ratios of Bi to red P (0, 1:10, 1:2, and 1:1) were also prepared. The samples were treated via thermal vaporization method. The capsules were heated to 550 °C at 5 °C per minute, held for 2 h, cooled to 300 °C (holding temperature) at 2 °C per minute and held for 10 h, and finally cool to room temperature at 2 °C per minute. After the reaction, the crystallized red P was washed with D.I. water and ethanol.

2.2. Photocatalytic test

A 300 W xenon lamp ($I = 18.3 \text{ A}$) with a 420 nm cut-off filter served as the visible light source. The photocatalytic H₂ evolution experiments were carried out in a closed gas system (Perfect light company) linked to gas chromatography (GC 7900, Techcomp). 20 mg of the sample was dispersed in the solution of 45 mL D. I. water and 5 mL methanol (hole scavenger). 1 wt% Pt was loaded onto each sample by photo-reduction of H₂PtCl₆ [16,30]. After purged with argon to remove dissolved air, the suspension was irradiated by visible light. The amount of hydrogen evolved from photocatalytic water reduction was measured by Techcomp GC7900 gas chromatography with a capillary column (molecular sieve 5A') and a TCD detector. High purity argon gas was used as a carrier gas. In the photocatalytic degradation of methyl orange (MO), 10 mg sample was dispersed in 30 mL 100 ppm MO aqueous solution. The suspension was magnetically stirred in dark for 5 h to achieve adsorption/desorption equilibrium. Then the photocatalytic test was carried out under visible light illumination. At certain time intervals, 1.5 mL of the suspension was taken and centrifuged. The absorbance of the supernatant was measured at 485 nm using an UV-vis spectrophotometer (UV-2990, Shimadzu, Japan).

2.3. Photo-deposition of Pt and MnO_x

5 mg of PMBs was dispersed in 10 mL 0.1 M H₂PtCl₆ or 0.1 M MnSO₄ aqueous solution for the photo-reduction and the photo-oxidation of MnO_x, respectively) [31]. The suspensions were irradiated by a 300 W xenon lamp ($\lambda \geq 420 \text{ nm}$) for 2 h and then centrifuged. The precipitates

were collected and washed with DI water and ethanol. After drying, the samples were characterized by SEM (scanning electron microscope) and EDX (energy dispersive X-ray spectroscopy).

2.4. Photocurrent measurements

Electrodes were made by depositing the samples onto FTO conducting glass via the doctor blade method. 5 mg of the sample was ultrasonically dispersed in 100 μL 0.05% Nafion in ethanol. Then, the suspension was dropped onto an FTO glass and dried. Photocurrents were measured with a three-electrode cell where the sample of interest was the working electrode, with a platinum foil ($1.0 \times 1.0 \text{ cm}^{-2}$) as a counter electrode and a saturated potassium chloride silver chloride electrode (Ag/AgCl) as a reference electrode. The electrolyte chosen was 0.1 M Na₂SO₄. A 300 W xenon arc lamp coupled with an AM 1.5 G global filter (100 mW cm^{-2}) was used as a radiation source. A UV cut-off filter ($\lambda > 420 \text{ nm}$) was used to simulate the visible light. The transient photocurrent was measured by a CHI 760E electrochemical workstation.

2.5. Theoretical calculations

VASP computational package was used for all the calculations in this article [32]. We applied projector-augmented-wave method with Perdew–Burke–Ernzerhof GGA functional [33–35]. Electronic convergence limit was set to be $1 \times 10^{-4} \text{ eV}$. Van der Waals d2 correction was taken into account [36]. Optimization of atomic coordinates was considered to be converged if Hellmann–Feynman force was smaller than $5 \times 10^{-2} \text{ eV \AA}^{-1}$. Bulk Hittorf's P and a slab exposing (013) facet are constructed. The slab consists of 42 phosphorus atoms. All the atoms are relaxed during optimization. The vacuum region is about 15 Å in height. We applied Monkhorst–Pack scheme $3 \times 3 \times 1$ for k -point selection and resulted in 5 irreducible k -points.

3. Results and discussion

3.1. Catalyst characterization

As shown in Fig. 1a, the PMBs are about 10 μm in width, 100 μm in length and about 0.3 μm in thickness. The XRD pattern of PMBs is well indexed to Hittorf's P (JCPDS: 44-0906) (Fig. 1b). The inset illustrates that the high peak at 15.66 relates to the (013) facet (Fig. 1b), while the corresponding peak at is quite low in the standard XRD pattern predicted from the crystal structure. The difference in the peak intensity indicates the orientation of the particular facets in the crystal. The peaks marked by asterisks are indexed to elemental Bi (JCPDS: 44-1246). Its Raman spectrum (Fig. 1c) exhibits clear peaks compared with that of amorphous red P. The Raman spectrum of the PMBs differs from that of Fibrous P [26] due to the difference in structure. Fibrous P and Hittorf's P are both constituted by covalently linked phosphorus pentagonal tubes that consist of alternating P₈ and P₉ cages linked by a P₂ chelating bridge. The P tubes in Hittorf's P are arranged perpendicular to each other, whereas those in Fibrous P are parallel (Fig. S1a and b) [17,29,37,38]. Absorption spectra of PMBs and amorphous red P are shown in Fig. S2a. The band gaps of PMBs and amorphous red P are 1.3 eV and 1.5 eV, respectively, measured by Tauc plots converted from their absorption spectra (Fig. S2b and c).

The as-prepared PMBs are in high crystallinity. The detailed crystal nature of the PMBs is further investigated by high-resolution transmission electron microscopy (HRTEM). Fig. 1d shows the HRTEM image of a corner of a PMB, while the inset shows the orientation of the PMB. As shown in Fig. 1e, the well-resolved interference fringe along the edge has a spacing of 5.67 Å, which agrees well with the interplanar distance between (013) planes of Hittorf's P. The selected area electron diffraction (SAED) pattern of an individual PMB reveals that the short edge and the long edge are (013) and (400) facet, respectively. The

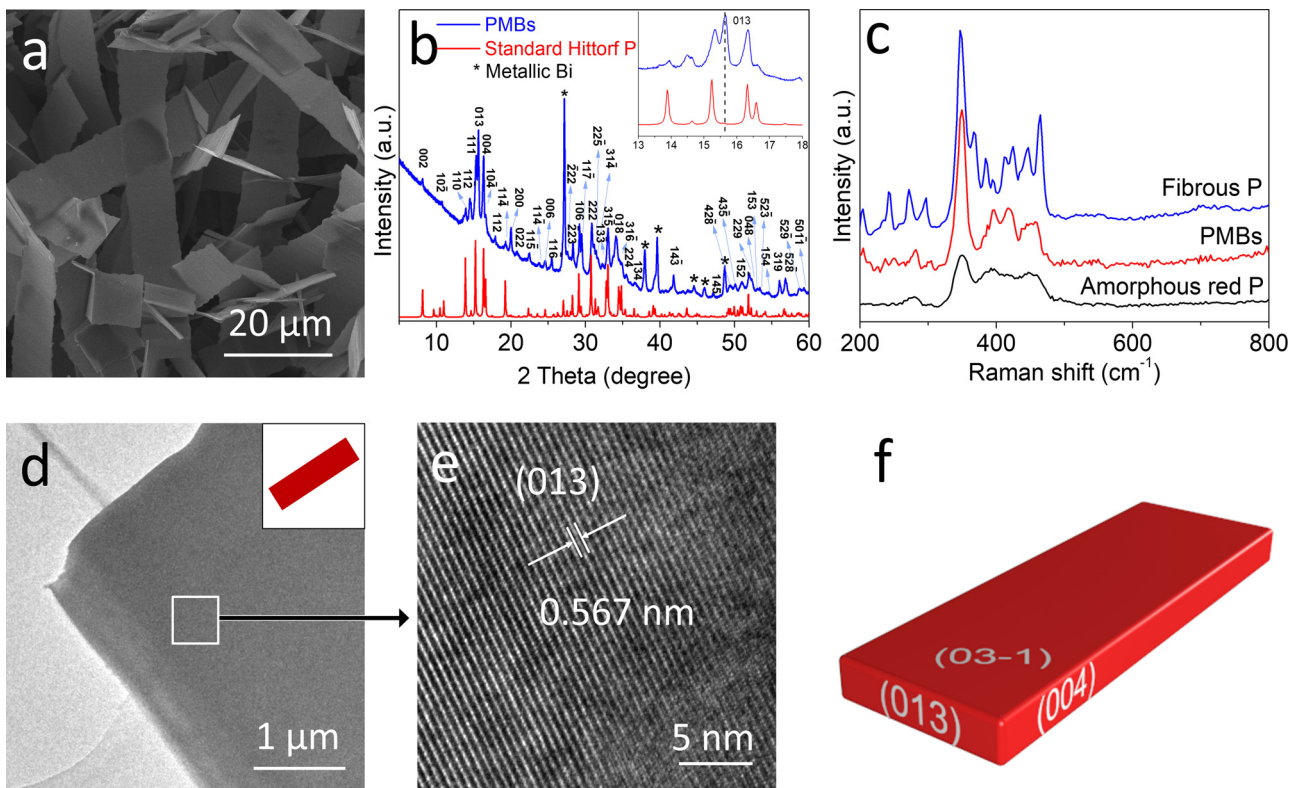


Fig. 1. (a) SEM image of PMBs. (b) XRD pattern of PMBs compared with the standard pattern of Hittorf's P. (d) Raman spectra of PMBs, Fibrous P and amorphous red P. (d) and (e) HRTEM patterns of a PMB. The (013) planes (spacing, 0.567 nm) are oriented parallel to the edge. (f) Three facets of the PMB.

plane of the PMBs is calculated to be (03-1) (see Fig. S3, Tables S1-2, and Formula S1-2 for details). The three exposed facets were shown in Fig. 1f.

3.2. Proposed growth mechanism of PMBs

Different substrates have been used to grow different crystalline P. For example, type-II P preferentially grows on the α -Ti wafer; Fibrous P tends to form on Si nanowire wafer or SiO_2 fiber [26,28].

Some reports have shown that liquid metal can promote the crystal growth. The high mobility of atoms on liquid metal surfaces may erase the nucleation vacancies and eliminate the grain boundaries, thereby leading to more homogeneous nucleation and the formation of large-scale single crystalline materials. For instance, large-scale single crystal graphene can be fabricated on the surface of molten copper [39–41], CdTe [42] quantum wires and ZnSe nanowires [43] could be synthesized on Bi nanodroplets.

We propose that liquid Bi plays an indispensable role in the growth of the PMBs. The morphology of the P crystal highly depends on the amount of Bi, as shown in the control experiments (Fig. S4). The microbelts cannot be formed without Bi. The PMBs generated with $\text{Bi:P} = 1:10$ are about 15 μm in width, which is wider than that from $\text{Bi:P} = 1:5$. In the presence of excessive Bi, the red P is hard to evaporate because it is surrounded by liquid metal. Fig. S5b shows the capsule after heating with $\text{Bi:P} = 1:1$ in it. The P is trapped by Bi and cannot spread to the whole capsule. This is different from that with $\text{Bi:P} = 1:5$ shown in Fig. S5a. Therefore, microbelts were hardly obtained with too much Bi (Fig. S5b), and the XRD pattern in Fig. S6 indicates the poor crystallinity of the sample.

Based on the studies above, we propose a mechanism for the formation of PMBs initiated by Bi nanodroplets (Fig. 2). (a) Bi and amorphous red P powder are sealed in vacuum quartz capsule to avoid oxidation. (b) When the precursors are elevated to 550 °C, amorphous red P sublimes while Bi melt as its melting point is 271 °C [44]. At

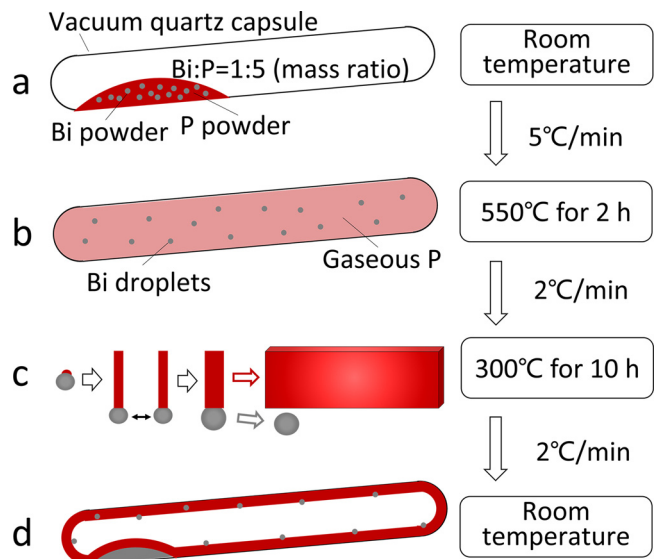


Fig. 2. The growth of PMBs initiated by liquid Bi via thermal vaporization. (a) Bi powder and amorphous red P with a mass ratio of 1:5 were put into a vacuum quartz capsule. (b) P vaporized while Bi melted to a liquid phase at 550 °C; (c) When the temperature decreased to 300 °C and held for 10 h, PMBs were grown initiated by Bi droplets. (d) Bi and P condensed after the capsule cooled to room temperature.

550 °C, molecule motion of P vapor becomes more and more violent and cause fast turbulence inside the capsule, which lashes the metal droplets, stretching them into smaller ones. The Bi nanodroplets then tend to form in the spherical shape due to the high surface tension of liquid metal [45]. (c) The temperature is then declined to 300 °C and held for 10 h, the vaporized P was adsorbed by Bi nanodroplets and

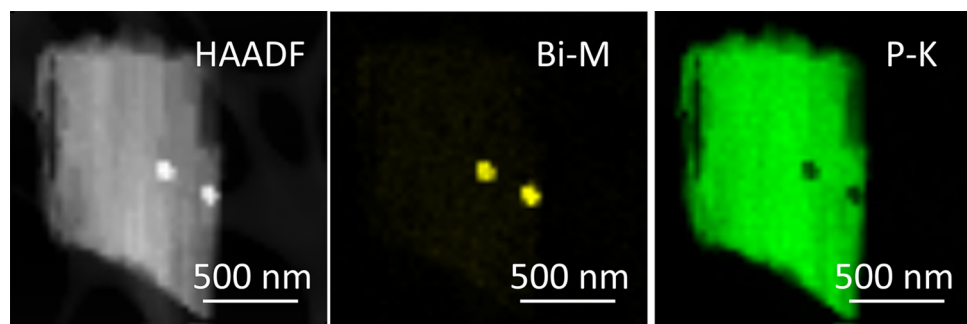


Fig. 3. Elemental mapping of the PMB with Bi nanodroplets.

nucleates on the surface of the droplets to form the seed crystals, which then grow to nanorods [42]. Carrying the P rods, Bi nanodroplets coalesce to reduce the surface energy, in the meanwhile the nanorods cohere to form a thicker one. The crystal then grows to a microbelt, while the Bi nanodroplet may leave the belt. (d) The system was cooled to room temperature, during which majority of Bi nanodroplets agglomerate [45,46], while some droplets coagulate individually on the PMBs result from the abrupt temperature drop. The Bi nanoparticles were found on some PMBs as shown in the TEM (transmission electron microscopy) image in Fig. S7, confirmed the elemental mapping pattern (Fig. 3). According to TGA (Fig. S8), P accounts for 60 wt% in the product. XPS spectrum (Fig. S9) of P 2p shows that most of P is in elemental state (peaks at 130.07 and 130.77 eV), while the surface of the PMB is partially oxidized in the atmosphere (peaks at 134.67 eV). If P reacted with Bi, it would be negatively charged, which is reflected by an XPS peak less than 130 eV. However, no signal is detected at energy lower than 130 eV, which reveals that P did not react with Bi.

3.3. Photocatalytic performance

The visible-light-driven H₂ production of the samples is shown in Fig. 4a. The H₂ evolution rate of PMBs in the sample is calculated to be 513.3 μmol g⁻¹ h⁻¹, which is about ten times higher than that of the amorphous red P (49.2 μmol g⁻¹ h⁻¹). The morphology and crystal

structure remained intact after the photocatalytic reaction as displayed in the SEM and XRD patterns in Fig. S10. The effect of precursor composition on the photoactivity of the PMBs was studied (Fig. S11). Bi:P = 1:10 also performs well in photocatalytic H₂ formation because of the specific microbelt structure, while P without Bi and samples with excessive Bi in precursors have lower photoactivity.

Fig. 4b illustrates the activity of the removal of MO over the PMBs and amorphous red P under visible light. The apparent degradation rate constant, k, can be calculated by the equation $k = \ln(C_0/C)/t$ [47]. C₀ is the MO concentration after adsorption/desorption equilibrium point before irradiation. C is the MO concentration at the irradiation time, t. The degradation rate of MO over PMBs ($k = 0.05878$) has a six-fold improvement than that over amorphous red P ($k = 0.00934$).

The enhanced photocatalytic activity is also confirmed by photocurrent response of the samples under on-off illumination cycles. Electrodes fabricated from PMBs and amorphous red P both show repeatable cathodic photocurrents upon visible illumination at -0.6 V vs. RHE (Fig. 4c). The photocurrent density of PMBs ($\Delta J = 15 \mu\text{A}/\text{cm}^2$) is much larger than that of amorphous red P ($\Delta J = 2 \mu\text{A}/\text{cm}^2$), indicating the higher transfer efficiency of photoexcited charge carriers in PMBs.

Since the PMBs contain residual Bi, the effect of Bi on the photocatalytic activity must be investigated. Fig. 4a indicates that pure Bi powder is photoinactive. To confirm that Bi does not contribute to H₂ evolution, the photocurrent of an electrode containing amorphous red P

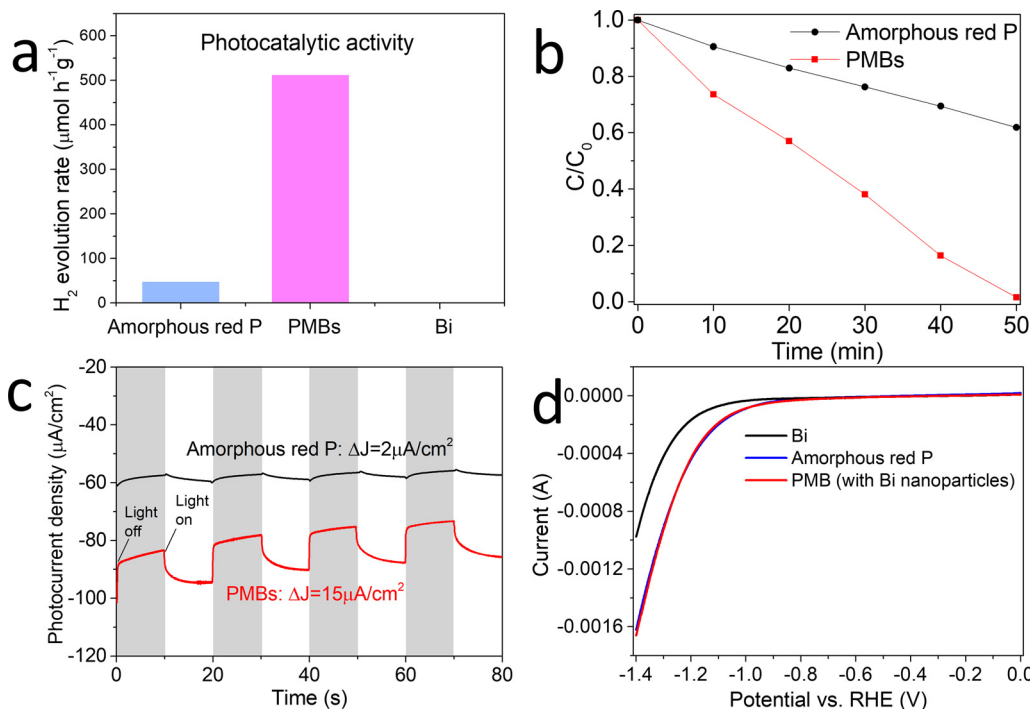


Fig. 4. (a) The activity of visible-light-driven H₂ evolution on different photocatalysts. (b) The degradation of MO over PMBs and amorphous red P. (c) Photocurrent response of PMBs and amorphous red P to on-off cycles of visible illumination at 10 s intervals with a bias potential of -0.6 V vs. RHE. (d) Cathodic polarization curves of Bi, amorphous red P, and PMBs.

and Bi was measured. The electrode was fabricated by using the adhesive Nafion with 5 mg amorphous red P and 2 mg Bi powder (see Experimental part 2.4 for details). Then the photocurrent plots of the mixture and the pure amorphous red P were recorded at -0.6 V vs. RHE. The same photocurrent of about $2.5 \mu\text{A}/\text{cm}^2$ was obtained (Fig. S12), indicating that the presence of Bi would not improve the charge transformation. It is therefore reasonable to conclude that Bi is not involved in the photocatalysis process. Fig. 4d shows the cathodic polarization curves of Bi, amorphous red P, and PMBs. A higher cathodic current and earlier onset potential mean that H_2 is formed more easily. The curves of amorphous red P and PMBs overlap with each other but the cathodic current of Bi is much weaker. That means Bi cannot kinetically enhance H_2 evolution. Results from Fig. 4 clearly suggest that Bi does not contribute to the H_2 production. The function of Bi is just to initiate the growth of PMBs, and its presence in the final product does not improve the performance of the photocatalyst.

3.4. Charge polarization

The charge polarization effect in the crystal is confirmed by photo-reduction deposition of Pt. PtCl_4^{6-} will be reduced to elemental Pt by the electrons generated from the photocatalyst. Thus, Pt particles tend to form on electron rich regions [31]. As shown in SEM images (Fig. 5a and b) and EDX spectra (Fig. S13a and b), Pt and MnO_x particles are selectively deposited onto the short edges and the middle of the PMBs, respectively, after two hours of visible-light illumination. A reasonable explanation is that the photoexcited electrons generated inside the crystal preferentially move to and accumulate on the short edge ((013) facets), and then reduce H_2PtCl_6 to Pt particles, while the holes migrate to the middle of PMBs. It also demonstrates that (013) facets are the active facets for photocatalytic H_2 evolution since the photoexcited electrons on (013) facets are ready to reduce H^+ to H_2 (Fig. 5c). For comparison, Pt particles were also deposited on amorphous red P. Fig. S14 shows only random distribution of on the irregular surface of the sample. Thus, there is no charge polarization in the amorphous red P.

The charge polarization effect in PMBs can also be proved in the surface potential distribution detected by Kelvin Probe Force Microscope (KPFM) (Fig. 5e). The topography image taken by atomic force microscopy (AFM) is shown in Fig. 5d. Under the illumination of 532 nm laser, the surface potential in the middle of the PMB became

higher than in the dark, while the potential on the short ends became lower. The potential change on the PMB surface indicates that photo-excited electrons move to the ends, leaving the holes in the middle. In photocatalysis, the unique electronic polarization and electron distribution in the PMBs result in less charge recombination and higher charge transfer efficiency and higher utilization rate of photocarriers. Hence the photocatalytic activity of PMBs is significantly improved. The work function is 4.8 eV, measured by KPFM with Au as the reference.

The preferential migration of electrons in the PMBs is studied by first-principles calculation according to density functional theory (Fig. 6a-d). In addition to bulk Hittorf's P, we also establish a slab exposing (013) facets (Figs. 6a, b, and S15), which is the active facet for the photocatalytic H_2 evolution. An obvious bandgap can be observed in the total density of states (DOS) and band diagram of bulk Hittorf's P (Fig. 6c), confirming its semiconductive property. The highest-energy state of the VB and the lowest-energy state of the CB are vertically aligned, which means the electron can be excited from VB to CB without a change in crystal momentum (k -vector). This suggests that P is a direct transition semiconductor. The bandgap about 1.6 eV is close to the previously reported value [23]. Whereas on the slab of (013), the conduction (CB) becomes a little lower and the bandgap is slightly narrower (Fig. 6d). Besides, three intermediate states (IS) appear in the bandgap. They are denoted as IS-1, IS-2, and IS-3 from the top of CB to the bottom of the valence band (VB). Under illumination, electrons can be excited to these IS easily using photons with lower energy (Fig. S16) [48]. A full VB to CB transition can be achieved step-by-step through these IS [49], thereby increasing the light absorption and utilization of photons [50,51]. Besides, due to the lower energy level of the IS, other photoexcited electrons generated inside the PMBs are expected to preferentially move to the (013) facets, which is a possible reason to explain why (013) is the active facet in PMBs. (Fig. S17)

The band-decomposed charge density iso-surface of the electronic states was performed to study the spatial charge distribution at CB, IS and VB energy levels. (Fig. 6e) As shown in Fig. S15, the vertical direction is the [013] orientation, and the bottom and top planes are the (013) facets according to crystal symmetry. The charges at an energy level of VB distributed uniformly around the unit cell. By contrast, those at CB are sparse in the center of the unit cell but concentrate at the (013) facet. When electrons are excited to the CB, they are more likely

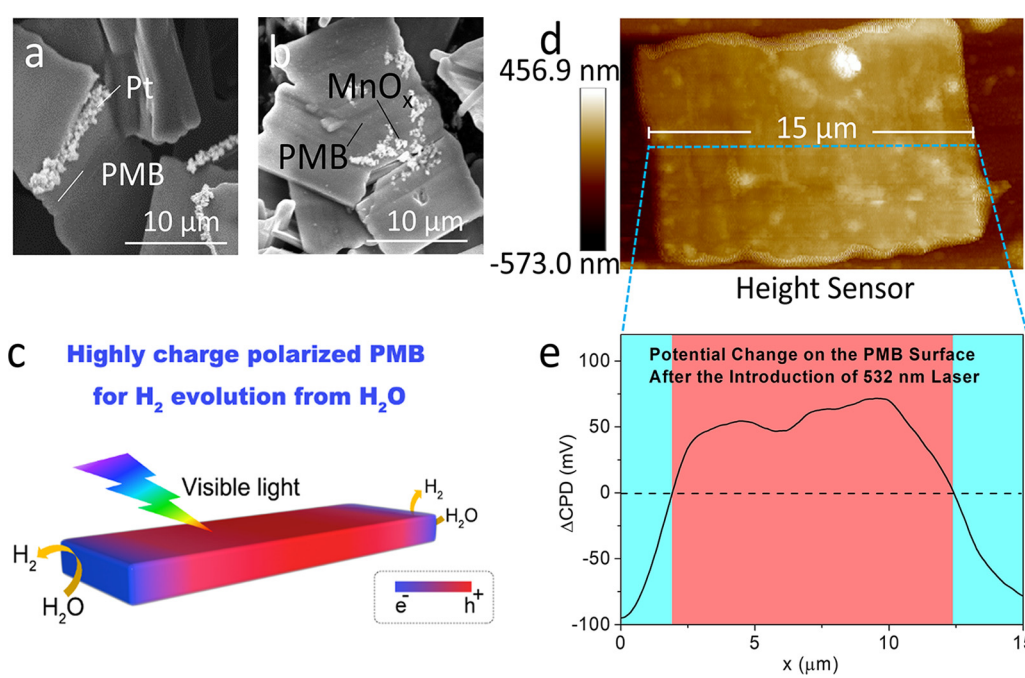


Fig. 5. SEM images of photo-deposition of Pt (a) and MnO_x (b) on the PMBs. (c) Schematic for H_2 evolution from H_2O over the highly charge polarized PMB. (d) AFM image of a PMB. (e) Surface potential change after the introduction of 532 nm laser. (ΔCPD is the contact potential difference of the PMB section between in light and dark, detected by KPFM).

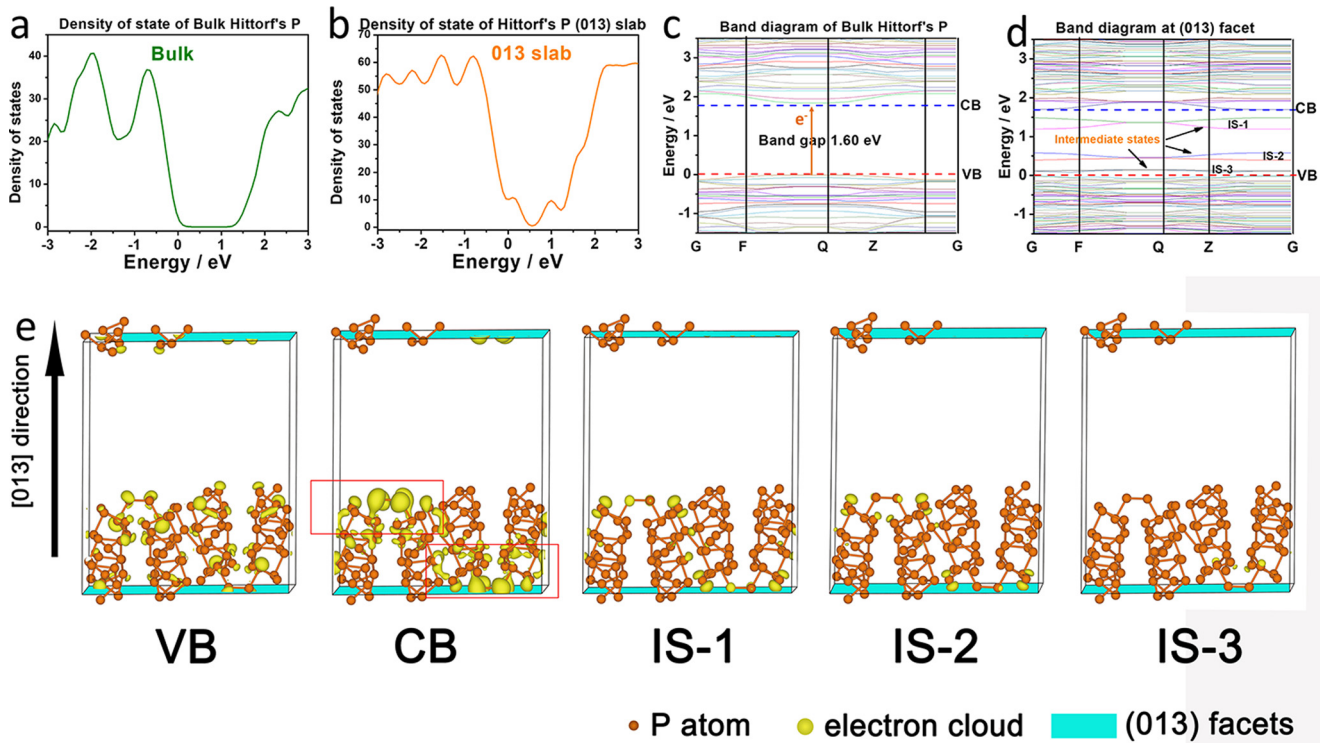


Fig. 6. Density of states (DOS) of (a) Bulk and (b) (013) slab of Hittorf's red P. Band structure of (c) Bulk and (d) (013) slab of Hittorf's red P. There are three intermediate states (IS) between CB and VB of the (013) slab. (e) Decomposed charge density iso-surface for valence band (VB) edge, conduction band (CB) edge, and three IS.

to accumulate on the (013) facets spatially. This is in good agreement with the Pt photo-deposition experiment.

The intermediate states, also known as trap states, are confirmed by femtosecond transient absorption spectrum (TAS) as Fig. 7, which can investigate the charge carrier dynamics of PMBs. The spectra were measured using 400 nm pump with a laser pulse of ca. 50 fs duration (3.1 eV, larger energy than the red P band gap of 1.69 eV). A white light continuum of 450–750 nm was used as a probe. Fig. 7a shows the TAS of PMBs at different delay times. After 400 nm illumination, the curves rise from 1 ps to 10 ps, but then fall. Similarly, in the time-resolved TAS shown in the Fig. 7b, the initial dramatical rise at the time scale < 10 ps can be observed at different wavelengths, followed by the decrease after 10 ps. The rise of the signal should be due to the photoexcitation of electrons from the ground state (GS) to the emissive state (EM) in PMBs [52]. Then, part of the electrons in the EM will recombine with holes in the GS, thereby leading to the decrease of the TAS signal. However, the trap states in the PMBs will “trap” part of the electrons from the GS. And it is reported that the recombination of these trapped electrons with holes happens in a relatively long time (10–1000 s) [53]. As a result, for curves after 100 ps in Fig. 7a, the broad and continuous negative absorption can be observed at the range of 450–700 nm. And the curves in Fig. 7b drop to be negative from 100 ps.

According to literature, the negative value corresponds to hole bleaching caused by trapped electrons [54,55]. Therefore, the internal cause of the charge polarization is that the photo-excited electrons are trapped by the intermediate states of (013) facets and aggregate on the short edges of the PMBs so that the holes are left in the middle.

By adjusting the holding temperature during the synthesis, the morphology and crystal structure of the red P can be controlled (Figs. S18 and S19). P microrods and microfibers can be obtained when the reaction was held at 400°C and 500°C for 10 h, respectively.

4. Conclusions

In summary, we have synthesized highly charge polarized single crystalline red PMBs with exposed active (013) facets on a liquid Bi substrate by a simple thermal vaporization method. Under visible light irradiation, photocatalytic H₂ evolution rate of PMBs is about ten times higher than that of amorphous red P. The high photocatalytic activity of Hittorf's PMBs is attributed to the unique charge polarization and distribution of photoexcited electron. This is the first observation of photo-induced charge polarization in elemental photocatalysts. This work may shed new light on the future development of high-efficiency P-based photocatalytic devices and systems.

Acknowledgements

The authors thank Dr. Quan Li and Ms. Danni Lan for the help in collecting and analyzing the elemental mapping and the SAED images, and Dr. Jianbin Xu and Dr. Zefeng Chen for the help in KPFM analysis. This work was partially supported by grants from the Research Grants Council of the Hong Kong Special Administrative Region, China, under Theme-based Research Scheme through Project No. T23-407/13-N and Project No. 14305417. This work was also supported by a grant from the Vice-Chancellor's One-off Discretionary Fund of The Chinese University of Hong Kong (Project No. VCF2014016). The theoretical calculation is

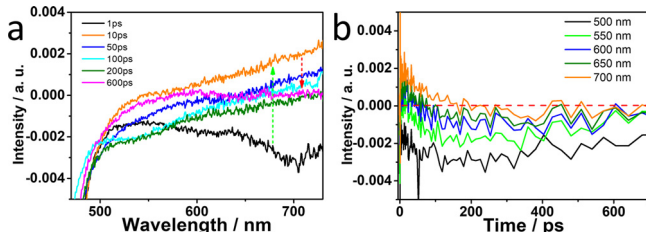


Fig. 7. (a) Wavelength-dependent TAS of PMBs at different time (b) Time profile of normalized transient absorption spectra at different wavelength.

supported by National Supercomputer Center in Guangzhou and National Supercomputing Center in Shenzhen (Shenzhen Cloud Computing Center).

Appendix A. Supplementary data

Supplementary material related to this article can be found, in the online version, at doi:<https://doi.org/10.1016/j.apcatb.2019.01.092>.

References

- [1] H.C. Pape, Annu. Rev. Physiol. 58 (1996) 299–327.
- [2] M. Biel, C. Wahl-Schott, S. Michalakis, X.G. Zong, Physiol. Rev. 89 (2009) 847–885.
- [3] X.Y. Huang, K.Q. Wang, Y.Z. Wang, B. Wang, L.L. Zhang, F. Gao, Y. Zhao, W.H. Feng, S.Y. Zhang, P. Liu, Appl. Catal. B 227 (2018) 322–329.
- [4] B. Zhang, H.P. Zhang, Z.Y. Wang, X.Y. Zhang, X.Y. Qin, Y. Dai, Y.Y. Liu, P. Wang, Y.J. Li, B.B. Huang, Appl. Catal. B 211 (2017) 258–265.
- [5] C.G. Zhou, J.K. Zhou, L. Lu, J.J. Wang, Z. Shi, B. Wang, L. Pei, S.C. Yan, Z.T. Yu, Z.G. Zou, Appl. Catal. B 237 (2018) 742–752.
- [6] H. Huang, Y. He, X. Li, M. Li, C. Zeng, F. Dong, X. Du, T. Zhang, Y. Zhang, J. Mater. Chem. A 3 (2015) 24547–24556.
- [7] H. Huang, X. Li, J. Wang, F. Dong, P.K. Chu, T. Zhang, Y. Zhang, ACS Catal. 5 (2015) 4094–4103.
- [8] H. Huang, S. Tu, C. Zeng, T. Zhang, A.H. Reshak, Y. Zhang, Angew. Chem. Int. Ed. 56 (2017) 11860–11864.
- [9] W. Ye, C.H. Ren, D.B. Liu, C.M. Wang, N. Zhang, W.S. Yan, L. Song, Y.J. Xiong, Nano Res. 9 (2016) 2662–2671.
- [10] H. Huang, X. Han, X. Li, S. Wang, P.K. Chu, Y. Zhang, ACS Appl. Mater. Interfaces 7 (2015) 482–492.
- [11] F. Chen, H. Huang, L. Ye, T. Zhang, Y. Zhang, X. Han, T. Ma, Adv. Funct. Mater. 28 (2018) 1804284.
- [12] H. Yu, J. Li, Y. Zhang, S. Yang, K. Han, F. Dong, T. Ma, H. Huang, Angew. Chem. Int. Ed. (2019).
- [13] H. Huang, K. Xiao, T. Zhang, F. Dong, Y. Zhang, Appl. Catal. B 203 (2017) 879–888.
- [14] H. Huang, K. Xiao, Y. He, T. Zhang, F. Dong, X. Du, Y. Zhang, Appl. Catal. B 199 (2016) 75–86.
- [15] M. Scheer, G. Balazs, A. Seitz, Chem. Rev. 110 (2010) 4236–4256.
- [16] B. Kraeutler, A.J. Bard, J. Am. Chem. Soc. 100 (1978) 2239–2240.
- [17] H. Thurn, H. Krebs, Acta Crystallogr. Sect. B: Struct. Crystallogr. Cryst. Chem. 25 (1969) 125–135.
- [18] M. Ruck, D. Hoppe, B. Wahl, P. Simon, Y. Wang, G. Seifert, Angew. Chem. Int. Ed. 44 (2005) 7616–7619.
- [19] Z. Shen, Z. Hu, W. Wang, S.F. Lee, D.K. Chan, Y. Li, T. Gu, J.C. Yu, Nanoscale 6 (2014) 14163–14167.
- [20] P. Bridgman, J. Am. Chem. Soc. 36 (1914) 1344–1363.
- [21] M.S. Zhu, C.Y. Zhai, M. Fujitsuka, T. Majima, Appl. Catal. B 221 (2018) 645–651.
- [22] W.C. Chang, K.W. Tseng, H.Y. Tuan, Nano Lett. 17 (2017) 1240–1247.
- [23] F. Wang, W.K.H. Ng, C.Y. Jimmy, H. Zhu, C. Li, L. Zhang, Z. Liu, Q. Li, Appl. Catal. B 111 (2012) 409–414.
- [24] L. Li, Y. Yu, G.J. Ye, Q. Ge, X. Ou, H. Wu, D. Feng, X.H. Chen, Y. Zhang, Nat. Nanotechnol. 9 (2014) 372–377.
- [25] M. Buscema, D.J. Groenendijk, S.I. Blanter, G.A. Steele, H.S. Van Der Zant, A. Castellanos-Gomez, Nano Lett. 14 (2014) 3347–3352.
- [26] Z. Hu, L. Yuan, Z. Liu, Z. Shen, J.C. Yu, Angew. Chem. 128 (2016) 9732–9737.
- [27] X. Zhu, T. Zhang, Z. Sun, H. Chen, J. Guan, X. Chen, H. Ji, P. Du, S. Yang, Adv. Mater. 29 (2017) 1605776.
- [28] Z. Shen, Z. Hu, W. Wang, S.-F. Lee, D.K. Chan, Y. Li, T. Gu, C.Y. Jimmy, Nanoscale 6 (2014) 14163–14167.
- [29] Z. Hu, Z. Shen, C.Y. Jimmy, Green Chem. 19 (2017) 588–613.
- [30] X. Wang, K. Maeda, A. Thomas, K. Takanabe, G. Xin, J.M. Carlsson, K. Domen, M. Antonietti, Nat. Mater. 8 (2009) 76–80.
- [31] R.G. Li, F.X. Zhang, D.G. Wang, J.X. Yang, M.R. Li, J. Zhu, X. Zhou, H.X. Han, C. Li, Nat. Commun. 4 (2013) 1432.
- [32] G. Kresse, J. Furthmuller, Phys. Rev. B 54 (1996) 11169–11186.
- [33] P.E. Blochl, Phys. Rev. B 50 (1994) 17953–17979.
- [34] G. Kresse, D. Joubert, Phys. Rev. B 59 (1999) 1758–1775.
- [35] J.P. Perdew, K. Burke, M. Ernzerhof, Phys. Rev. Lett. 77 (1996) 3865–3868.
- [36] F. Bachhuber, J. von Appen, R. Dronskowski, P. Schmidt, T. Nilges, A. Pfleiderer, R. Weilrich, Z. Krist.-Cryst. Mater. 230 (2015) 107–115.
- [37] M.E. Barr, B.R. Adams, R.R. Weller, L.F. Dahl, J. Am. Chem. Soc. 113 (1991) 3052–3060.
- [38] T. Wiegand, H. Eckert, S. Grimme, D. Hoppe, M. Ruck, Chem. Eur. J. 17 (2011) 8739–8748.
- [39] D.C. Geng, B. Wu, Y.L. Guo, L.P. Huang, Y.Z. Xue, J.Y. Chen, G. Yu, L. Jiang, W.P. Hu, Y.Q. Liu, Proc. Natl. Acad. Sci. U. S. A. 109 (2012) 7992–7996.
- [40] W.I. Park, J. Ceram. Process. Res. 9 (2008) 666–671.
- [41] A. Mohsin, L. Liu, P. Liu, W. Deng, I.N. Ivanov, G. Li, O.E. Dyck, G. Duschner, J.R. Dunlap, K. Xiao, ACS Nano 7 (2013) 8924–8931.
- [42] F.D. Wang, W.E. Buhr, ACS Nano 11 (2017) 12526–12535.
- [43] X.W. Zhang, J.S. Jie, X.J. Zhang, F.J. Yu, J. Mater. Chem. C 4 (2016) 857–862.
- [44] Y. Wang, Y. Xia, Nano Lett. 4 (2004) 2047–2050.
- [45] J.J. Li, Z.C. Wang, F.L. Deepak, ACS Nano 11 (2017) 5590–5597.
- [46] Y.X. Li, B.R. Bunes, L. Zang, J. Zhao, Y. Li, Y.Q. Zhu, C.Y. Wang, ACS Nano 10 (2016) 2386–2391.
- [47] Y. Yu, C.Y. Jimmy, C.-Y. Chan, Y.-K. Che, J.-C. Zhao, L. Ding, W.-K. Ge, P.-K. Wong, Appl. Catal. B 61 (2005) 1–11.
- [48] Y. Wang, J. Cheng, S. Yu, E.J. Alcocer, M. Shahid, Z. Wang, W. Pan, Sci. Rep. 6 (2016) 32711.
- [49] R. Lucena, J.C. Conesa, I. Aguilera, P. Palacios, P. Wahnon, J. Mater. Chem. A 2 (2014) 8236–8245.
- [50] H. Pan, Nanoscale Res. Lett. 9 (2014) 531–531.
- [51] H. Pan, Y.W. Zhang, Nano Energy 1 (2012) 488–493.
- [52] Y. Yang, M. Forster, Y. Ling, G. Wang, T. Zhai, Y. Tong, A.J. Cowan, Y. Li, Angew. Chem. Int. Ed. 55 (2016) 3403–3407.
- [53] L. Jing, R.X. Zhu, D.L. Phillips, J.C. Yu, Adv. Funct. Mater. 27 (2017) 1703484.
- [54] M. Barroso, S.R. Pendlebury, A.J. Cowan, J.R. Durrant, Chem. Sci. 4 (2013) 2724–2734.
- [55] B. Pattengale, J. Ludwig, J. Huang, J. Phys. Chem. C 120 (2016) 1421–1427.